


















LETTER TO THE EDITOR

Evolution of dynamic fibrils from the cooler chromosphere to the hotter corona[★]

Sudip Mandal¹, Hardi Peter¹, Lakshmi Pradeep Chitta¹, Sami K. Solanki^{1,2}, Regina Aznar Cuadrado¹,
Udo Schühle¹, Luca Teriaca¹, Juan Martínez-Sykora⁹, David Berghmans⁵, Frédéric Auchère⁶,
Susanna Parenti⁶, Andrei N. Zhukov^{5,7}, Éric Buchlin⁶, Cis Verbeeck⁵, Emil Kraaikamp⁵,
Luciano Rodriguez⁵, David M. Long¹⁰, Krzysztof Barczynski^{3,4}, Gabriel Pelouze⁶, and Philip J. Smith⁸

¹ Max Planck Institute for Solar System Research, Justus-von-Liebig-Weg 3, 37077 Göttingen, Germany
e-mail: smandal.solar@gmail.com

² School of Space Research, Kyung Hee University, Yongin, Gyeonggi 446-701, Republic of Korea

³ Physikalisch-Meteorologisches Observatorium Davos, World Radiation Center, 7260 Davos Dorf, Switzerland

⁴ ETH-Zürich, Wolfgang-Pauli-Str. 27, 8093 Zürich, Switzerland

⁵ Solar-Terrestrial Centre of Excellence – SIDC, Royal Observatory of Belgium, Ringlaan -3- Av. Circulaire, 1180 Brussels, Belgium

⁶ Université Paris-Saclay, CNRS, Institut d'Astrophysique Spatiale, 91405 Orsay, France

⁷ Skobel'syn Institute of Nuclear Physics, Moscow State University, 119991 Moscow, Russia

⁸ UCL-Mullard Space Science Laboratory, Holmbury St. Mary, Dorking, Surrey RH5 6NT, UK

⁹ Bay Area Environmental Research Institute, Moffett Field, CA, USA

¹⁰ Astrophysics Research Centre, School of Mathematics and Physics, Queen's University Belfast, University Road, Belfast BT7 1NN, Northern Ireland, UK

Received 3 July 2023 / Accepted 8 September 2023

ABSTRACT

Dynamic fibrils (DFs) are commonly observed chromospheric features in solar active regions. Recent observations from the Extreme Ultraviolet Imager (EUI) aboard the Solar Orbiter have revealed unambiguous signatures of DFs at the coronal base in extreme ultraviolet (EUV) emission. However, it remains unclear if the DFs detected in the EUV are linked to their chromospheric counterparts. Simultaneous detection of DFs from chromospheric to coronal temperatures could provide important information on their thermal structuring and evolution through the solar atmosphere. In this paper, we address this question by using coordinated EUV observations from the Atmospheric Imaging Assembly (AIA), Interface Region Imaging Spectrograph (IRIS), and EUI to establish a one-to-one correspondence between chromospheric and transition region DFs (observed by IRIS) with their coronal counterparts (observed by EUI and AIA). Our analysis confirms a close correspondence between DFs observed at different atmospheric layers and reveals that DFs can reach temperatures of about 1.5 million Kelvin, typical of the coronal base in active regions. Furthermore, the intensity evolution of these DFs, as measured by tracking them over time, reveals a shock-driven scenario in which plasma piles up near the tips of these DFs and, subsequently, these tips appear as bright blobs in coronal images. These findings provide information on the thermal structuring of DFs and their evolution and impact through the solar atmosphere.

Key words. Sun: corona – Sun: chromosphere – Sun: magnetic fields – Sun: UV radiation – Sun: transition region – Sun: atmosphere

1. Introduction

Dynamic fibrils (DFs), one of the prominent chromospheric features of solar active regions, are characterised by their dark, elongated, jet-like appearance in the wings and core of $H\alpha$ (Rutten 2007). They are thought to be closely related to the quiet-Sun type-I spicules and they are likewise shock-driven phenomena (De Pontieu et al. 2004; Hansteen et al. 2006). Considering their ubiquitous presence, it is a natural next step to consider whether hotter counterparts of these DFs exist at coronal temperatures. So far, reports of such signatures at coronal temperatures are very sparse. For example, Skogsrud et al. (2016) reported bright rim-like parabolic structures (indicative

of DFs) in space–time plots derived using coronal data from the Atmospheric Imaging Assembly (AIA; Lemen et al. 2012). However, they could not reliably identify the bright features that produced those parabolic traces in the first place, primarily due to the inadequate spatial resolution of AIA (image scale of ~ 430 km pixel⁻¹). The 174 Å High-Resolution Imager of the Extreme Ultraviolet Imager (EUI; Rochus et al. 2020) on board Solar Orbiter (Müller et al. 2020) has overcome this limitation by providing high-resolution, high-cadence extreme ultraviolet (EUV) observations. Using EUI data (with an image scale of ~ 135 km pixel⁻¹), Mandal et al. (2023) reported the first unambiguous detection of DFs at the coronal base of an active region. Small bright blobs of sizes ~ 0.5 Mm² within the EUV moss features of that active region were found to be moving back and forth with time, producing parabolic tracks in space–time maps.

[★] Movies associated to Figs. 4, C.2 and C.3 are available at <https://www.aanda.org>

The properties of these blobs matched well with earlier studies of chromospheric DFs (e.g., [De Pontieu et al. 2007](#)). Therefore, [Mandal et al. \(2023\)](#) hypothesised that the observed bright blob-like features were the hot tips of cooler chromospheric DFs.

Nevertheless, the question of whether the bright blob-like features reported in [Mandal et al. \(2023\)](#) are of coronal origin ($\log T = 6$) or of a cooler transition region plasma ($\log T = 5.4$), remained open. This is largely because: (a) the response functions of these coronal imagers span a wide range of temperature and they often have a secondary peak at lower temperature alongside the high-temperature primary peak and (b) there were no lower temperature diagnostics available for the EUV dataset used by [Mandal et al. \(2023\)](#); therefore, there was no possibility to independently verify the temperature structure of DFs. In this work, we used co-ordinated EUV, AIA, and IRIS (Interface Region Imaging Spectrograph IRIS; [De Pontieu et al. 2014](#)) observations and followed the evolution of DFs from the chromosphere to the lower corona. Our results hint towards a more comprehensive understanding of DF evolution than has been achieved thus far, while also providing insights into their thermal structuring.

2. Data

The EUV dataset was taken by the 174 Å High Resolution Imager (HRI_{EUV}) of EUV on 2022-03-17, between 03:23:08 UT and 04:08:05 UT, with a cadence of 3 s (part of the SoI/O/EUV Data Release 5.0; [Mampaey et al. 2022](#)). At the time of this observation, Solar Orbiter was located at a distance of 0.379 AU from the Sun, therefore, one HRI_{EUV} pixel corresponds to 135 km on the solar surface. Moreover, the angle between the Sun-Solar Orbiter line and the Sun-Earth line was $\approx 26.4^\circ$. We complemented the EUV observation with co-temporal EUV data from AIA, onboard the Solar Dynamics Observatory (SDO; [Pesnell et al. 2012](#)). In particular, we used data from the AIA 171 Å channel, which samples the plasma of a similar temperature to HRI_{EUV}, but with a significantly lower spatial ($431 \text{ km pixel}^{-1}$) and temporal (12 s) resolution. To capture the lower temperature dynamics, we used coordinated slit-jaw imager (SJI) data from two channels of IRIS, namely, the 1400 and 2796 Å channels. These IRIS datasets have a cadence of 3.6 s and a pixel scale of 239 km (owing to its 2×2 spatial binning). Lastly, we corrected for the difference in light travel time between Sun-Solar Orbiter and Sun-SDO and all the time stamps quoted in this paper are Earth times.

Figure 1a shows an AIA 171 Å image from this observational campaign alongside the fields of view (FoVs) of HRI_{EUV} and IRIS, which are outlined via the cyan and red curves. The IRIS observations cover a part of the HRI_{EUV} FoV and, considering our aim of following the evolution of a DF simultaneously along different heights in the solar atmosphere, we restricted the AIA and HRI_{EUV} FoVs to match that of IRIS. Additionally, we re-projected the EUV data onto the IRIS FoV to take into account the angle of 26.4° between the Sun-Solar Orbiter and the Sun-Earth line (i.e., with AIA and IRIS). This re-projection was carried out using the WCS keywords (present in the data files) as outlined in [Thompson \(2006\)](#). The HRI_{EUV} image in Fig. 1d shows this re-projection. Moreover, as this re-projection relies on a photospheric radius, it may encounter line-of-sight issues for features at higher altitudes. However, low-lying features such as dynamic fibrils are expected to be the least affected by this issue.

3. Analysis and results

The coordinated EUV-AIA-IRIS observations were centred on the active region NOAA 12965, which was in its decaying phase ([Berghmans et al. 2023](#)). A variety of features such as coronal loops and low-lying filaments (in AIA-171 and HRI_{EUV}), spots, and moss (in IRIS-1400 Å and 2796 Å) are seen within the FoV.

3.1. Space-time ($X-T$) maps

To capture DFs and their evolution, we placed multiple artificial slits in and around the active regions as shown in Fig. 1. The slit positions were fixed after visually inspecting different locations within the FoV and then picking out the ones from which we have good signal in the IRIS channels. Each slit is 10 IRIS pixels wide ($\sim 2.4 \text{ Mm}$) and the final $X-T$ maps are derived after averaging emission over the respective slit widths. Furthermore, to enhance the appearance of bright structures, we subtracted the background (as calculated through a boxcar smoothing) along the transverse direction (i.e., along the y -axis) of an $X-T$ map. Figures 2 and 3 present these contrast-enhanced $X-T$ maps from six of these slits. Additionally, these maps with individual colourbars can be found in Appendix E.

The HRI_{EUV} $X-T$ maps in Figs. 2 and 3 are filled with bright, seemingly parabolic tracks that are basically EUV signatures of DFs ([Mandal et al. 2023](#)). Sometimes these tracks appear repetitive, highlighting the recurrent nature of DFs (for example, HRI_{EUV} Slit-1 $X-T$ map between $y = 7$ and 8 Mm). Since a given DF is associated with a given parabolic profile, it is difficult to say from these images whether the repetitive tracks were due to the same DF or different DFs that happen to be in close spatial proximity. Nonetheless, we fit a few of these HRI_{EUV} tracks¹ with parabolas (see [Mandal et al. 2023](#) for details of this fitting procedure) and the fitted curves are overplotted in cyan in each of these HRI_{EUV} maps. For a given slit, we then overplotted these fitted curves on all other $X-T$ maps, namely, the cyan curves in AIA and IRIS $X-T$ maps are the ones we fitted in the corresponding HRI_{EUV} $X-T$ maps. A closer look at each of these $X-T$ maps, immediately reveals that the visibility of these parabolic trajectories of the DFs is best in HRI_{EUV} (which has the highest spatial resolution), whereas for AIA-171, the trajectories are either less resolved and fainter or absent. For IRIS-1400 channel, the signal is more prominent, while for 2796 channel, it is mostly at the base of these trajectories. Depending upon their simultaneous appearance in different channels, we classified the observed DFs into the following four categories:

Category-I; visible only in HRI_{EUV}. An example of this is the curve X7 is given in Fig. 2. At first, it appears that DFs that have a small maximum height, namely, those that travel only a few Mm into the atmosphere are the ones that fall into this category. However, examples such as X1 and X3 that have average maximum heights but still lack signals in other channels, are exceptions to this narrative.

Category-II; visible only in HRI_{EUV}, AIA 171 and IRIS 1400 maps. Examples of such DFs are X5 and X8 in Fig. 2b and X12 and X15 in Fig. 3. There is, however, some diversity within this class. For example, in some cases, the bright track in IRIS-1400 is significantly brighter either at the beginning or at the end of

¹ We visually identified and selected these 41 tracks as they appear relatively prominent, both in part or as a whole. These selected set of tracks, as representative examples, sample each of the DF category. Figures 2 and 3 contain all 41 of these detected tracks.

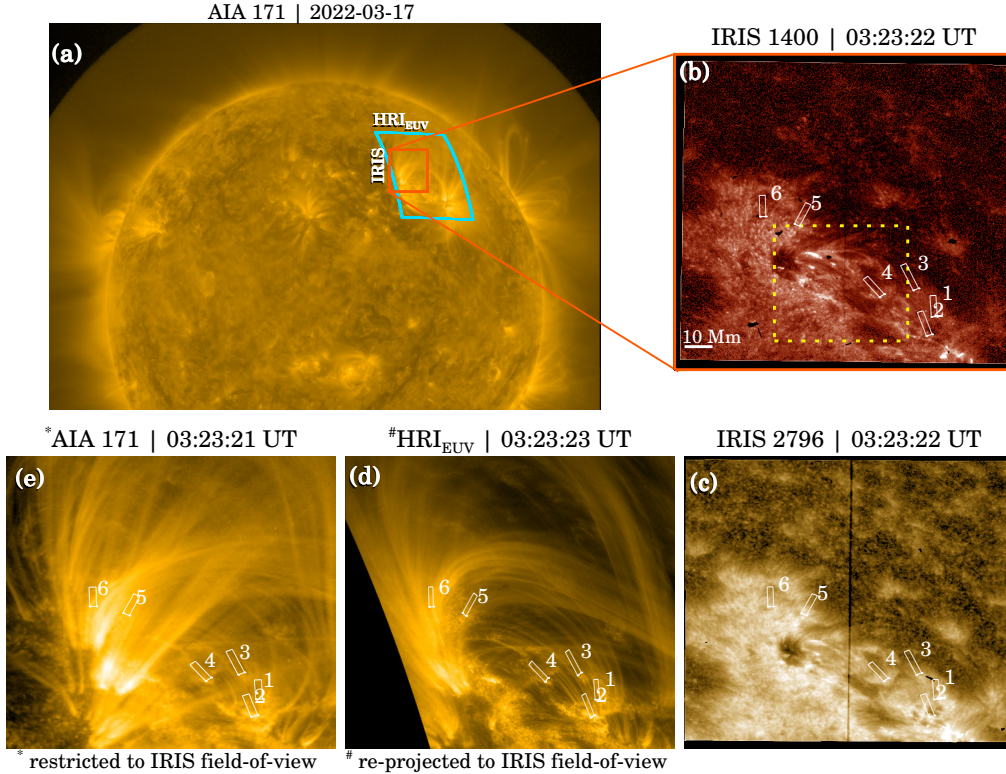


Fig. 1. Overview of the coordinated EUI-AIA-IRIS observation on 2022-03-17. Panel a shows the AIA 171 Å image in the background while the IRIS and EUI FoVs are marked by red and cyan rectangles, respectively. Panels b and c present the IRIS 1400 Å and 2796 Å slit jaw images, while panel d shows the EUI image after reprojecting it onto the IRIS FoV. Panel e shows the same but for AIA 171 Å channel (without reprojecting). The white boxes in panels b–e mark the locations of the artificial slits that are used to derive the space–time maps. The yellow box in panel b outlines the region analysed in Fig. D.1. Panels a–e are ordered clockwise.

the track (e.g., X8 or X15), while in other cases, it is uniformly bright throughout its whole extent (e.g., X5 or X12)².

Category-III; visible in all four channels. Although for these DFs we find a simultaneous signal in $X-T$ maps of all four channels, their signatures in the IRIS 2796 Å channel (and seldom in the IRIS 1400 Å channel) are either often faint or only localised to the footpoints of the tracks. There could be several factors affecting the appearance of a given DF in any IRIS passband, including the spectral and thermal characteristics of the filters. However, an investigation of these factors is beyond the scope of this paper. Nonetheless, the curve X9 in Fig. 2 and X11 in Fig. 3 are among the best examples of this category. The other ones such as X4, X6 of Fig. 2 and X10, X16, and X17 of Fig. 3 also fit in here despite their ambiguous appearance in the IRIS 2796 Å maps.

Category-IV; exceptions. This category contains examples that we could not fit into any of the previous three categories. For example, X2 in Fig. 2 has a clear visibility in HRI_{EUV} and 1400 channels (with some hints in the IRIS 2796 maps), but the signal in AIA 171 channel is (almost) non-existent. The other extreme example is the case in Fig. 3, where we see a (relatively) clear parabolic signal in 2796 channel (next to X10, between $t = 16$ and 20 min and $y = 6$ and 7 Mm, as highlighted by the arrow), while its signature in other channels is almost non-existent.

² This is not an artefact of the contrast enhancement procedure as the same trend is also visible in the original maps.

3.2. Temporal evolution of DF intensities

Having demonstrated that some DFs show signatures in different temperature regimes of the solar atmosphere, we go on to investigate their evolution by tracking their emission over time. Although it is possible to track a DF's temporal evolution by following the bright track that it creates in an $X-T$ map, we chose to do it by following a DF in every frame in a data sequence. The issue with the first approach has to do with the fact that the $X-T$ maps (as shown in Figs. 2 and 3) were produced after averaging over their slit widths; therefore, other features encroaching that slit will also contribute to the derived intensity³. Furthermore, it is also affected by the significant amount of overlap from other DFs as well. These issues, however, can be mitigated through latter method where one follows a DF in every frame avoiding overlaps. In order to make sure that we are following the same pixels in all four channels, we re-scaled the HRI_{EUV} and AIA data to match the IRIS resolution (effectively, this means up-scaling the AIA data and down-scaling the HRI_{EUV} data). Such re-scaling provides an added advantage that any pixel level mismatch in DF locations between HRI_{EUV} and IRIS (whether physical or due to re-projection of the HRI_{EUV} data) would also be taken care of in this process. Given its better signal-to-noise ratio (S/N) compared to other channels, we performed the feature tracking on the HRI_{EUV} images. Finally, the tracking was done visually, namely, by going through frame-by-frame and using the cursor to select the centre of a bright blob. We calculated the intensity of the detected feature as the mean of all the pixels within a circular

³ It is not practically possible to adjust the slit width so that it only follows a single DF over all frames.

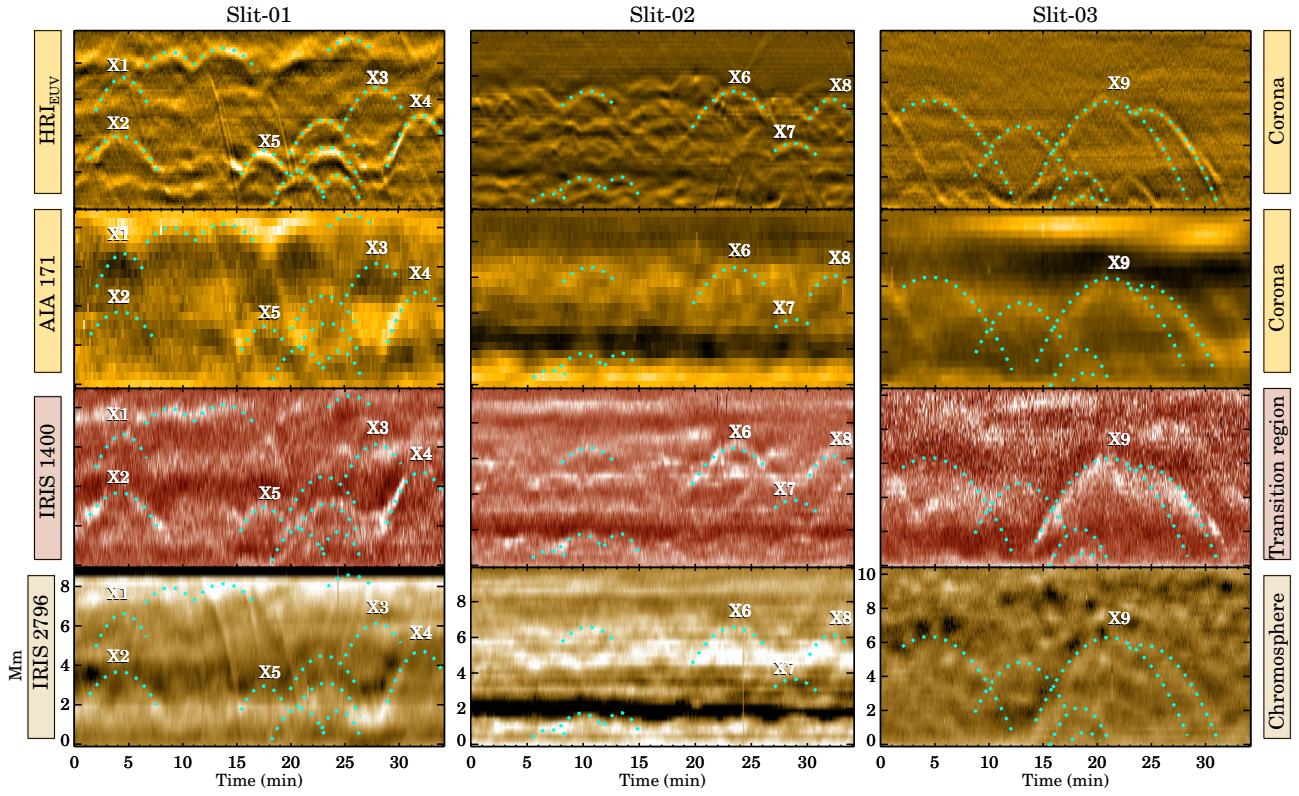


Fig. 2. Evolution of dynamic fibrils. Space-time ($X-T$) maps for slit-1 (left column), slit-2 (middle column), and slit-3 (right column) are displayed. The top $X-T$ map in each column is from the HRI_{EUV} data sequence, followed by the maps from AIA 171 Å, IRIS 1400 Å, and IRIS 2796 Å data. In each column, the cyan curves outline the parabolic fit to the bright tracks, as seen in the corresponding EUV $X-T$ map. Tracks marked with Letter ‘X’ are discussed further in Sect. 3.1.

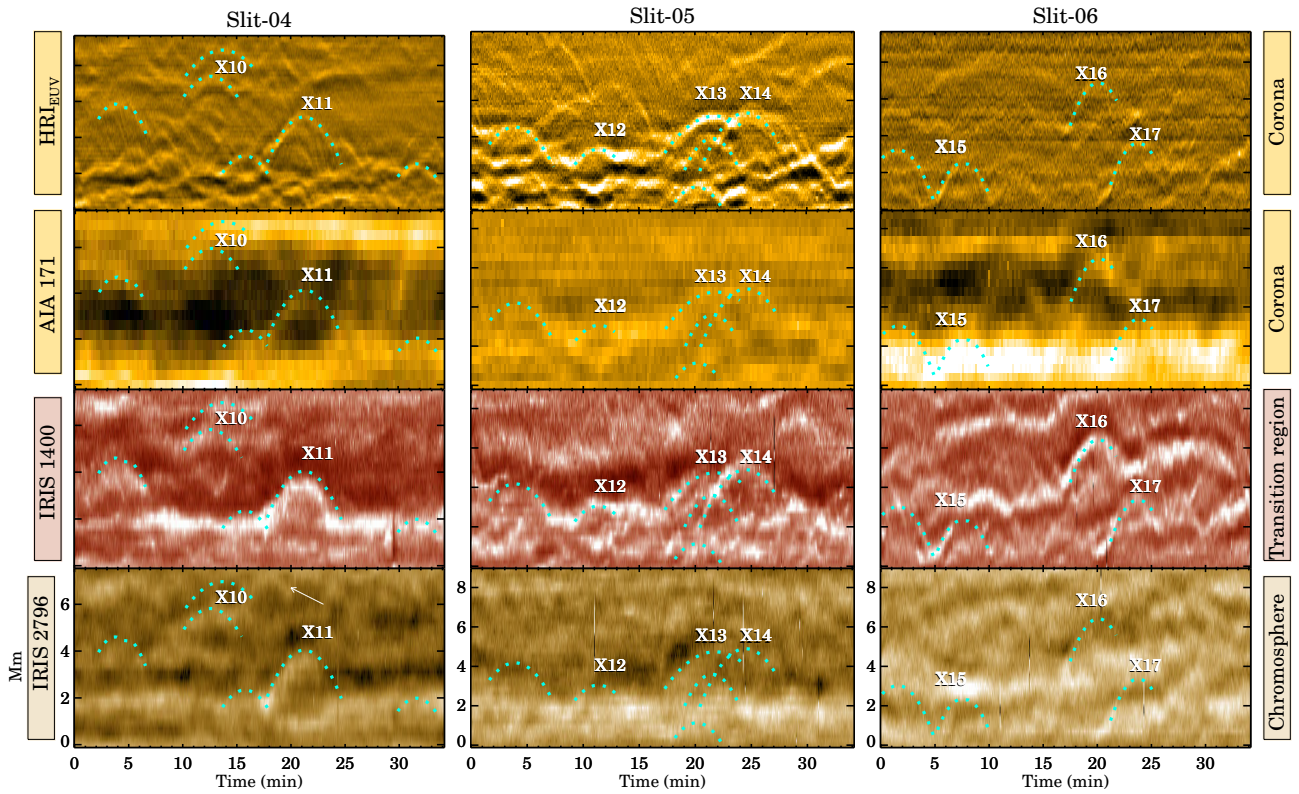


Fig. 3. Same as Fig. 2 but for slit-4 (left column), slit-5 (middle column), and slit-6 (right column). The arrow in the 2796 map of slit-4 points to a particular case discussed in Sect. 3.1.

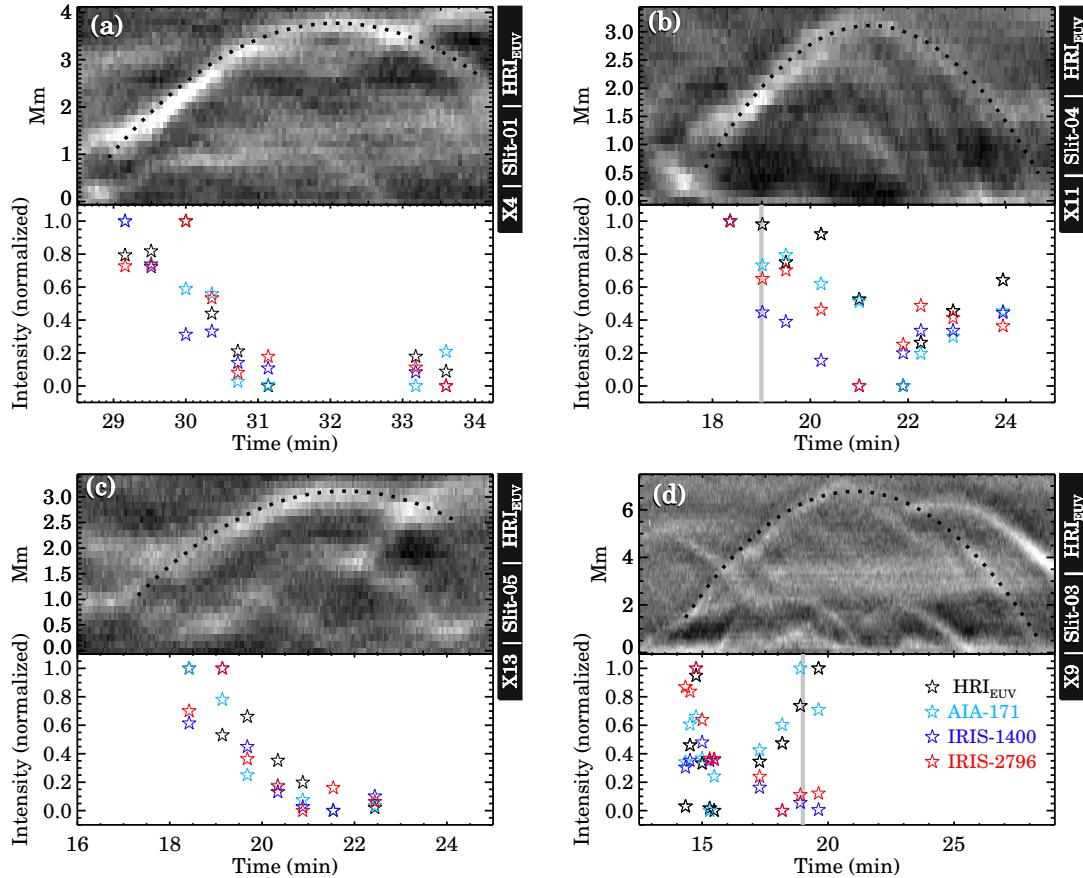


Fig. 4. Intensity evolution of four selected DFs. In panel a, the top section shows the HRI_{EUV} X - T maps (between $t = 28$ and 34 min) of slit-1, while the bottom section shows the evolution of intensities in four different imaging channels (HRI_{EUV} in black, AIA 171 Å in cyan, IRIS 1400 Å in blue and IRIS 2796 Å in red), of the DF that created the parabolic trajectory in the X - T map. The black dotted line in the top section is the parabolic fit to the observed bright track. Panels b–d show the same but for slit-4, slit-5, and slit-3. The grey vertical lines in panels b and d indicate the time when the emission measure analyses as those shown in Figs. 5 and A.1 are performed. Animations associated to this figure are available [online](#).

region encompassing the full extent of the blob (see the animation associated with Fig. 4 for more details). Once a DF has been traced in HRI_{EUV}, we used the same positional information to extract intensity values from the remaining three channels.

Figure 4 presents the intensity evolution of four selected DFs: three DFs from category III (panels a, b, and d) and one from category II (panel c). We see a common trend for cases shown in panels a, b, and c. The DF intensities in all four channels systematically decrease as it reaches its maximum height in its corresponding X - T map. However, once a DF starts receding (i.e., during the descending part of a parabola), there is a hint of intensity enhancements in all four channels. Nonetheless, the situation is quite different for the case shown in Fig. 4d, where we instead find a rapid drop in intensity at the beginning of the ascending phase (in line with the previous three cases). However, the situation changes quickly as the DF approaches its maximum height, where we see a systematic increase in HRI_{EUV} and AIA-171 intensities, whereas the IRIS-1400, 2796 intensities drop simultaneously. Unfortunately, we could not trace this DF beyond its maximum height due to substantial contribution from background (or foreground) features (see the associated movie). We do not include error estimates due to the photon Poisson (shot) noise, electronic readout noise, compression noise, or dark current noise associated to the derived intensities (statistical errors are not very useful here as the sample size is small in

each case). Nevertheless, the commonality and concurrency of the observed trends in intensities derived from data of different passbands of different instruments weigh in favour of the conclusion that the observed signal is of solar origin.

4. Discussion and conclusion

In this work, we set out to explore the connection between the lower-temperature chromospheric DFs with that of EUV DFs through coordinated HRI_{EUV}, AIA, and IRIS observations. Our results indicate strong correlations among them, both spatially and temporally. Below we highlight our main findings:

- The EUI X - T maps derived from moss-type regions are found to be filled with bright parabolic tracks that are indicative of DFs. Corresponding AIA X - T maps are also similarly populated while signatures of such tracks are less frequent in IRIS 1400 Å and 2796 Å data. We also note that the signal in 2796 Å channel is stronger near the start of these parabolic tracks, and some of the tracks in 1400 Å channel show a hint of spatial offset with the same in HRI_{EUV} data.
- There are several cases where we found simultaneous signal in HRI_{EUV}, AIA 171 Å, and IRIS 1400 Å channels. However, DF events where all four channels show co-spatial and co-temporal signals are infrequent.

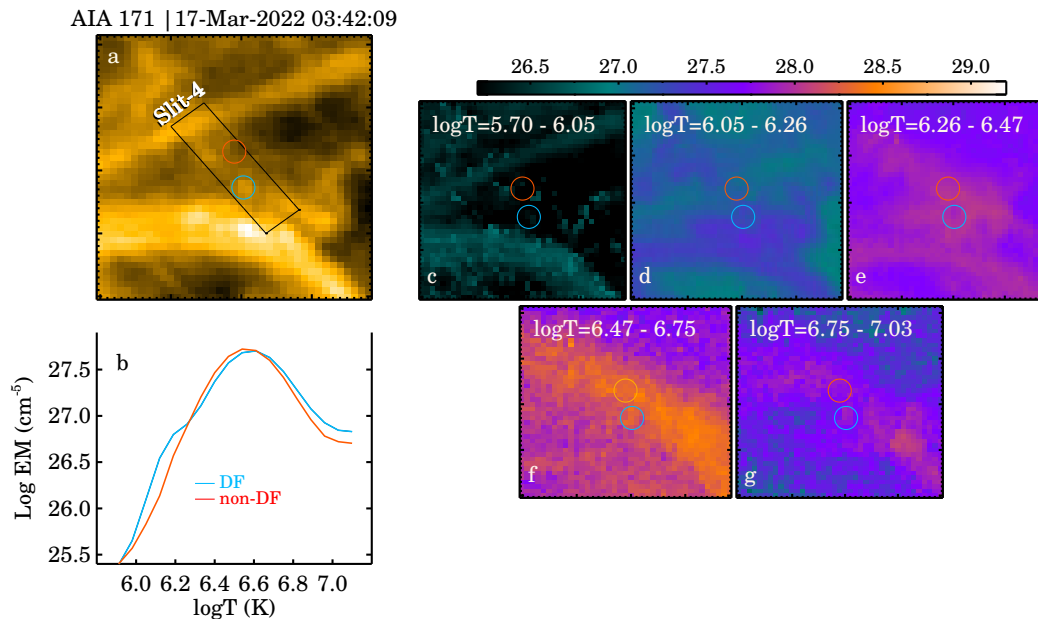


Fig. 5. Emission measure (EM) analysis of a DF. Panel a shows an AIA 171 Å image with the DF outlined by the cyan circle. The EM curve (derived at 03:42 UT) of the central pixel of that circle is shown in panel b (the blue curve), while the red curve shows the same but for a pixel away from the DF as outlined by the red circle in panel a. Panels c–g show 2D EM maps (of the FoV shown in panel a) at specific temperature bins, as noted in each panel.

- By following the evolution of four selected DFs, we found that the intensity of a DF tends to decrease as it travels upward in the atmosphere and, once the DF crosses its maximum height, its intensity starts to increase again. We, however, also found an example which is an exception to this scenario, therefore demonstrating the need for more statistics.

As mentioned in the introduction, DFs have traditionally been identified as a shock-driven phenomenon (De Pontieu et al. 2005; Hansteen et al. 2006). In this scenario, magnetoacoustic waves from the lower atmosphere steepen into shocks as they propagate upward and push the chromospheric material to higher heights to form a DF. If we now consider the bright blobs in HRI_{EUV} images as the hotter counterparts of the same chromospheric DFs, then we would expect to see a definite signature in IRIS channels for each bright track seen in HRI_{EUV} (or AIA) images. This is, however, not the case (as we can see in Figs. 2 and 3). There could be several reasons for the absence of such one-to-one correspondence: (1) A DF in the IRIS-2796 channel appears as more of an elongated diffuse structure as opposed to a bright blob that we found in other channels. Therefore, their visibility in an X-T map improves only if the DF is significantly brighter than the background. (2) Next, the properties of IRIS slit-jaw passbands also influence the visibility of these DFs. For example, the IRIS 1400 Å slit jaw imager passband is relatively wide (55 Å) and in non-flaring conditions, it is the Si I recombination continuum that contributes most to this channel (Martínez-Sykora et al. 2015). On the other hand, the 2796 Å bandpass is significantly narrower (5 Å), but the Mg II k line line is formed over a considerable range of heights and with strong non-local thermodynamic equilibrium conditions (Leenaarts et al. 2013). Therefore, DFs with lower contrast are barely detectable while the brightest ones remained visible. Furthermore, the IRIS dataset we used in this study has a 2 × 2 binning which results in a pixel scale of 0.33". Thus, the spatial binning of this IRIS data may also have played a role in the poor visibility of DFs. (3) Lastly, we recall that there exists a moderate angle of 26.4° between the two spacecraft (IRIS and Solar Orbiter). Hence,

different alignments of (magnetic) structures may have influenced their visibility across instruments.

Clues regarding the mechanism that possibly makes a chromospheric DF visible to higher temperature channels are given in Fig. 4. Those three cases where we see simultaneous decrement in intensity in all four channels can be explained through the following evolutionary scenario: the chromospheric material, propelled by the shock, travels upward and piles up material near the tip of the DF (similar to Fig. 5 of Bryans et al. 2016). This material pile-up enhances their visibility in the HRI_{EUV} and AIA 171 Å channels and this is also the reason behind their blob-like appearance in these channels. As the DF moves upward in the atmosphere, it constantly loses energy, primarily through radiation, with contributions from the thermal conduction and geometrical damping (fanning out of the magnetic field with height). Therefore, it explains why all four channels show a simultaneous intensity decrease. However, the reason why the intensity starts to increase as the DF starts to recede is not yet apparent. One possibility could be that the falling material gets adiabatically compressed against the denser chromospheric plasma, leading to a temperature increase in turn causing the emission enhancement. We cannot, however, rule out another possibility whereby the increase in intensity is simply due to enhanced density along the LOS. This evolutionary scenario matches well with the type-I spicules (Beckers 1968).

We note that the case shown in Fig. 4d exhibits a different evolution. Here, we postulate that the scenario in which the intensity of cooler channels drops and, simultaneously, the intensity of the hotter channels increases is similar to a type II spicule (De Pontieu et al. 2009). Spicules in general, undergo complex evolution across different atmospheric layers (Pereira et al. 2012), while type II ones often leave their imprints in transition region and coronal images (Roupe van der Voort et al. 2015; Samanta et al. 2019; Bose et al. 2021a). Numerical modelling works, such as those of Martínez-Sykora et al. (2018), reveal that these features are associated with magneto-acoustic shocks and flows; as a result, they also supply mass to coronal loops.

Nonetheless, type II is a subclass of spicules that reach greater heights and move faster. Furthermore, from the figure (Fig. 4), it is also evident that this particular DF shows a significantly larger height parameter (≈ 6 Mm) compared to other examples (≈ 3 Mm)⁴. Therefore, this may be an example of a EUV counterpart of a type-II spicule. However, at the same time, we are cautious about this conclusion because (a) it is based on a case which has a complicated evolutionary track with many overlapping structures (see the animation associated with Fig. 4) and (b) this DF could well be travelling nearly parallel to the solar surface such that higher height does not always mean higher altitude. Therefore, this needs further investigation. Future coordinated observations that include ground-based telescopes (specifically observations in a passband centred on $H\alpha$) would help in improving our understanding of the lower atmospheric evolution of these DFs.

Lastly, we discuss the possibility of a DF reaching typical coronal temperatures (\sim MK). To this end, we calculated the emission measure (EM) of DF plasma using the co-spatial and near-simultaneous multi-wavelength EUV data from AIA. We followed the inversion technique of Cheung et al. (2015). Figure 5 presents one such case (another case is shown in the appendix). The EM curve of the DF (outlined by the blue circle in panel a) is similar to a typical active region EM and it has a peak emission at $\log T$ of 6.6 (panel b), while a secondary hump is seen at $\log T = 6.2$. For comparison, we overplot (in red) the EM curve from a location away from the DF, as outlined by the red circle. Interestingly, the peak of the curve remains at $\log T = 6.6$, while the secondary hump seems to be absent in this case. However, we cannot draw a definitive conclusion on the exact temperature of the DF without a further investigation of the DEMs by tracking the DF over time, which is beyond the scope of this study. Nonetheless, at first glance, it appears that the DF is indeed reaching a temperature higher than 1 MK (≈ 1.5 MK). We further generated multiple 2D EM maps by dividing the entire temperature range into several bins (panels c–g). Through these maps, we found signatures of a hot loop nearly in the line of sight of the DF in question (panel f) and could probably be responsible for the observed primary peak at a higher temperature, while the DF itself might have a slightly lower temperature, but still slightly over 1 MK. Therefore, at least some DFs could well be considered as a source of coronal emission in active regions. Furthermore, recent studies on spicules, rapid blueshifted excursions (RBEs), and rapid redshifted excursions (RREs) also suggest that some of these features indeed show signatures in the transition region and coronal observations (Bose et al. 2021b; Vilangot Nhalil et al. 2022, 2023). As discussed earlier, since DFs are closely related to spicules, these studies align well with the results we find here (although some of these upper atmospheric signatures could also be due to type-II class spicules, e.g., as shown in Samanta et al. 2019, and may therefore be unrelated to DFs).

To conclude, by analysing coordinated HRI_{EUV}-IRIS-AIA observations of a moss-type region, we found a clear association between DFs that appear blob-like in HRI_{EUV} and IRIS-1400 data, with the DFs in the 2796 data that appear more as elongated, diffuse features. These DFs have a temperature of ≈ 1.5 MK, which reflects typical coronal values. A temporal analysis of their intensity evolution has revealed a scenario that is similar to type I spicules.

Acknowledgements. We thank the anonymous reviewer for the encouraging comments and helpful suggestions. Solar Orbiter is a space mission of interna-

tional collaboration between ESA and NASA, operated by ESA. The EUI instrument was built by CSL, IAS, MPS, MSSL/UCL, PMOD/WRC, ROB, LCF/IO with funding from the Belgian Federal Science Policy Office (BELSPO/PRODEX PEA 4000112292 and 4000134088); the Centre National d'Etudes Spatiales (CNES); the UK Space Agency (UKSA); the Bundesministerium für Wirtschaft und Energie (BMWi) through the Deutsches Zentrum für Luft- und Raumfahrt (DLR); and the Swiss Space Office (SSO). We are grateful to the ESA SOC and MOC teams for their support. Solar Dynamics Observatory (SDO) is the first mission to be launched for NASA's Living With a Star (LWS) Program. The data from the SDO/AIA consortium are provided by the Joint Science Operations Center (JSOC) Science Data Processing at Stanford University. IRIS is a NASA small explorer mission developed and operated by LMSAL with mission operations executed at NASA Ames Research Center and major contributions to downlink communications funded by ESA and the Norwegian Space Centre. L.P.C. gratefully acknowledges funding by the European Union (ERC, ORIGIN, 101039844). Views and opinions expressed are however those of the author(s) only and do not necessarily reflect those of the European Union or the European Research Council. Neither the European Union nor the granting authority can be held responsible for them. D.M.L. is grateful to the Science Technology and Facilities Council for the award of an Ernest Rutherford Fellowship (ST/R003246/1). A.N.Z. and L.R. thank the Belgian Federal Science Policy Office (BELSPO) for the provision of financial support in the framework of the PRODEX Programme of the European Space Agency (ESA) under contract numbers 4000136424 and 4000134474. J.M.S. gratefully acknowledges support by NASA grants 80NSSC18K1285, 80NSSC20K1272, 80NSSC21K0737, 80NSSC21K1684, 80NSSC23K0093 and contract NNG09FA40C (IRIS) and NNH19ZDA0130 (MUSE).

References

- Anfinogenov, S. A., Nakariakov, V. M., & Nisticò, G. 2015, *A&A*, **583**, A136
 Beckers, J. M. 1968, *Sol. Phys.*, **3**, 367
 Berghmans, D., Antolin, P., Auchère, F., et al. 2023, *A&A*, **675**, A110 (SO Nominal Mission Phase SI)
 Bose, S., Joshi, J., Henriques, V. M. J., & Rouppe van der Voort, L. 2021a, *A&A*, **647**, A147
 Bose, S., Rouppe van der Voort, L., Joshi, J., et al. 2021b, *A&A*, **654**, A51
 Bryans, P., McIntosh, S. W., De Moortel, I., & De Pontieu, B. 2016, *ApJ*, **829**, L18
 Cheung, M. C. M., Boerner, P., Schrijver, C. J., et al. 2015, *ApJ*, **807**, 143
 De Pontieu, B., Erdélyi, R., & James, S. P. 2004, *Nature*, **430**, 536
 De Pontieu, B., Erdélyi, R., & De Moortel, I. 2005, *ApJ*, **624**, L61
 De Pontieu, B., Hansteen, V. H., Rouppe van der Voort, L., van Noort, M., & Carlsson, M. 2007, *ApJ*, **655**, 624
 De Pontieu, B., McIntosh, S. W., Hansteen, V. H., & Schrijver, C. J. 2009, *ApJ*, **701**, L1
 De Pontieu, B., Title, A. M., Lemen, J. R., et al. 2014, *Sol. Phys.*, **289**, 2733
 Hansteen, V. H., De Pontieu, B., Rouppe van der Voort, L., van Noort, M., & Carlsson, M. 2006, *ApJ*, **647**, L73
 Heggland, L., De Pontieu, B., & Hansteen, V. H. 2007, *ApJ*, **666**, 1277
 Leenaarts, J., Pereira, T. M. D., Carlsson, M., Uitenbroek, H., & De Pontieu, B. 2013, *ApJ*, **772**, 90
 Lemen, J. R., Title, A. M., Akin, D. J., et al. 2012, *Sol. Phys.*, **275**, 17
 Mampaey, B., Verbeeck, F., Stegen, K., et al. 2022, *Solo/EUIData Release 5.0 2022-04*, <https://doi.org/10.24414/2qfw-tr95>
 Mandal, S., Chitta, L. P., Antolin, P., et al. 2022, *A&A*, **666**, L2
 Mandal, S., Peter, H., Chitta, L. P., et al. 2023, *A&A*, **670**, L3 (SO Nominal Mission Phase SI)
 Martínez-Sykora, J., Rouppe van der Voort, L., Carlsson, M., et al. 2015, *ApJ*, **803**, 44
 Martínez-Sykora, J., De Pontieu, B., De Moortel, I., Hansteen, V. H., & Carlsson, M. 2018, *ApJ*, **860**, 116
 Müller, D., St. Cyr, O. C., Zouganelis, I., et al. 2020, *A&A*, **642**, A1
 Okamoto, T. J., & De Pontieu, B. 2011, *ApJ*, **736**, L24
 Pereira, T. M. D., De Pontieu, B., & Carlsson, M. 2012, *ApJ*, **759**, 18
 Pesnell, W. D., Thompson, B. J., & Chamberlin, P. C. 2012, *Sol. Phys.*, **275**, 3
 Rochus, P., Auchère, F., Berghmans, D., et al. 2020, *A&A*, **642**, A8
 Rouppe van der Voort, L., De Pontieu, B., Pereira, T. M. D., Carlsson, M., & Hansteen, V. 2015, *ApJ*, **799**, L3
 Rutten, R. J. 2007, in *The Physics of Chromospheric Plasmas*, eds. P. Heinzel, I. Dorotovič, & R. J. Rutten, *ASP Conf. Ser.*, **368**, 27
 Samanta, T., Tian, H., Yurchyshyn, V., et al. 2019, *Science*, **366**, 890
 Skogsrud, H., Rouppe van der Voort, L., & De Pontieu, B. 2016, *ApJ*, **817**, 124
 Thompson, W. T. 2006, *A&A*, **449**, 791
 Verwichte, E., Nakariakov, V. M., Ofman, L., & Deluca, E. E. 2004, *Sol. Phys.*, **223**, 77
 Vilangot Nhalil, N., Shetye, J., & Doyle, J. G. 2022, *MNRAS*, **515**, 2672
 Vilangot Nhalil, N., Shetye, J., & Doyle, J. G. 2023, *MNRAS*, **524**, 1156

Appendix A: Further examples of EM analysis

In Fig. A.1, we present an additional example of the EM analysis on a DF. This particular DF is located within slit-3. The EM curve in this example (panel b) peaks at $\log T = 6.6$ and appears similar to the curve presented in Fig. 5 (b), although the secondary hump at $\log T = 1.2$ is not as pronounced as before. Unlike the previous case, the temperature binned 2D EM maps (panels c-g) do not show any blob-like structure but rather a dif-

fuse emission near the peak temperature, covering the whole FoV. We present further examples of EM analysis in Fig. A.2, which contains examples from slits-1, 2, and 6. Through these, we find that some DFs show signatures of a secondary peak around $\log T = 1.2$ (e.g. slit-2), while others do not (e.g. slit-6). Therefore, it further emphasises the need for a detailed statistical investigation exploring the contribution of the foreground and background structures to the derived EM curve (and its temporal evolution).

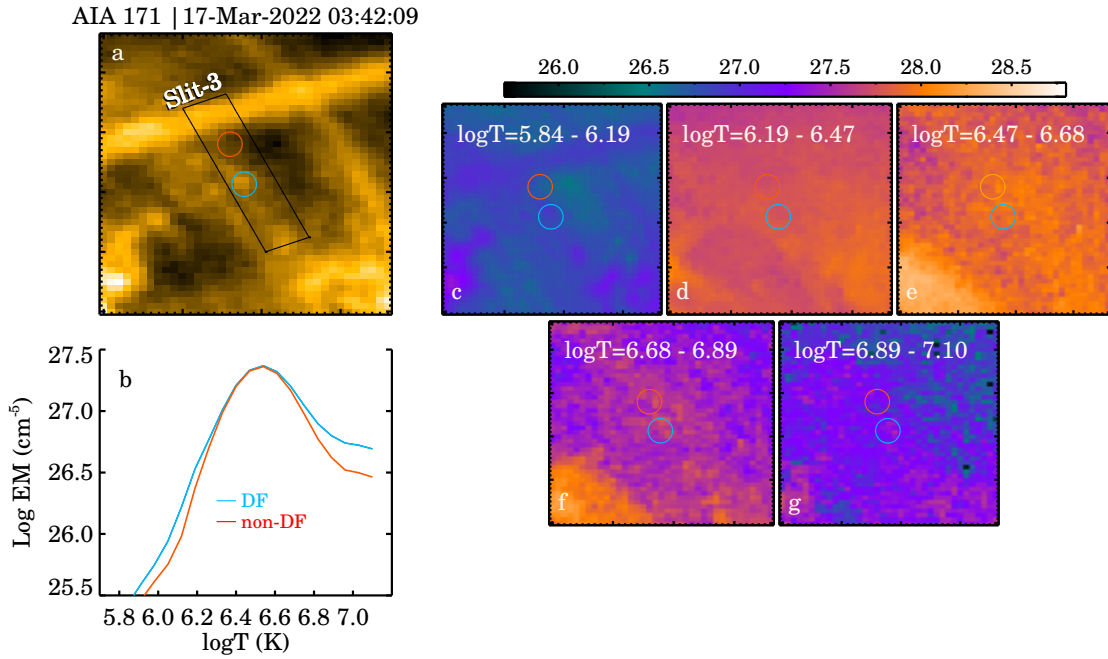


Fig. A.1. Same as Fig. 5 but for a different DF (from slit-3).

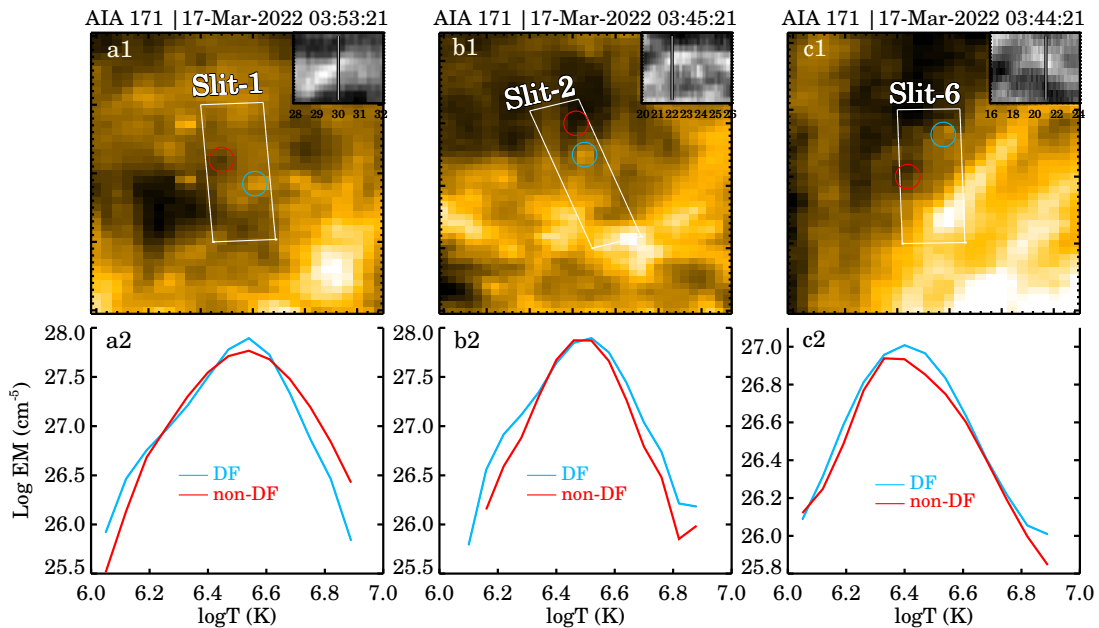


Fig. A.2. Additional examples of EM analysis of DFs. Panel descriptions are same as in Fig. 5. The tracks that those DFs create in AIA 171 maps are shown in insets of panels a1, b1, and c1. The vertical lines in these inset panels highlight when the EM measurement was carried out.

Appendix B: Correlation analysis

Inter-relationships between DF parameters (such as lifetime, apparent speed, travelled length, etc.) contain information about their generation mechanism (De Pontieu et al. 2007). Following the methodology outlined in Mandal et al. (2023), we derived the DF length as the maximum height of the parabola and DF lifetime as the time between the two ends of the parabola (after extrapolating the fitted curve to make it symmetric). In Fig. B.1, we show such scatter plots for this study. The correlation coefficients we obtained here are similar to those quoted in Mandal et al. (2023) and in agreement with the theoretical work by Heggland et al. (2007). There is, however, more to this story. Three DFs from slit-3 (the dark green symbols) appear as ‘outliers’ in all these scatter plots. A quick look at Fig. 2 reveals these ‘outlier’ DFs are the ones with large tracks and longer lifetimes. Although all parameters of these three DFs are substan-

tially different from other DFs, their maximum speeds seem to be not so extravagantly different. One possible explanation of such behaviour could be related to the inclination of local magnetic field and the periodicity of the driver as found in a numerical simulation by Heggland et al. (2007). These authors found that although an inclined field hosts a stronger driver (owing to lower acoustic cutoff; De Pontieu et al. 2004; Hansteen et al. 2006), it does not necessarily translate into higher maximum speed as this larger driving only leads to larger dissipation. Therefore, these seemingly outlier points that we find in our study, could well be cases with larger inclined field geometry. As we noted earlier, multiple overlappings and atypical evolution of these DFs (with X9 from Fig. 2 being one of them) might have an influence on their derived parameters. There is also the complexity of projection effects that may play a role on our results. Therefore, we need to investigate further, most likely with other EUI datasets of equal or better resolution than the one we used in this study.

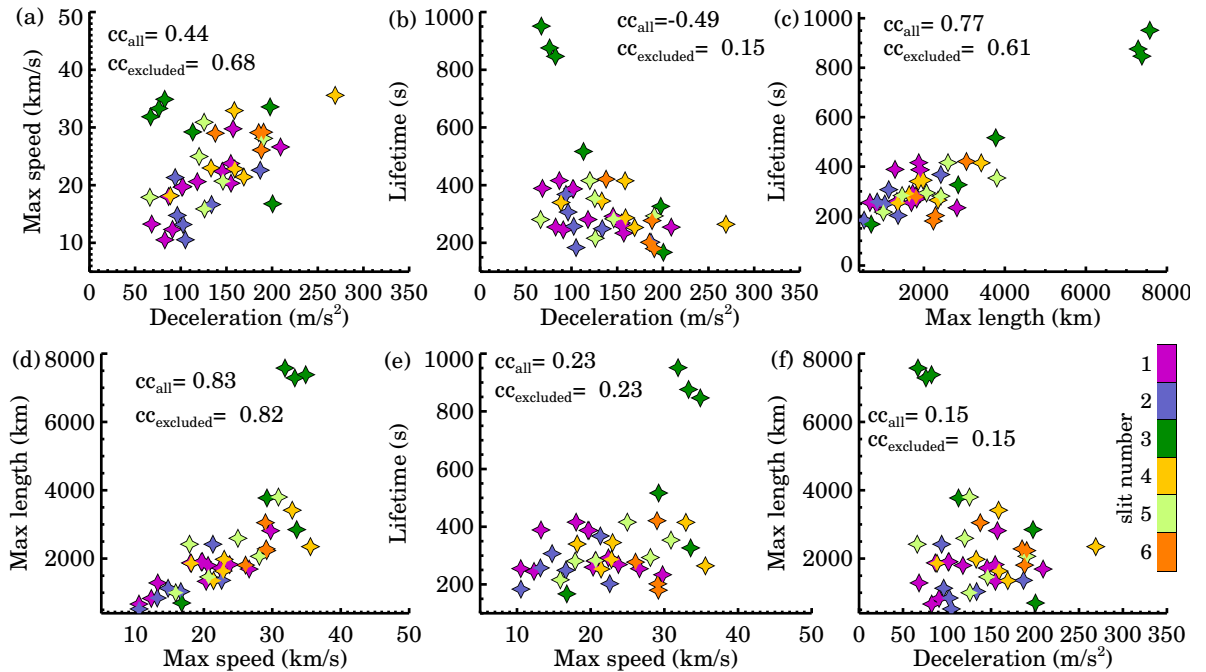


Fig. B.1. Inter-relationships between different DF parameters. Data from different slits are represented by a colour scheme, as noted in panel f. The correlation coefficients calculated with all data points (cc_{all}) and excluding three outlier points ($cc_{excluded}$) are also printed on each panel. See text for more details.

Appendix C: Zoomed-in images and evolution of DFs

We first present a zoomed-in view of the context image (Fig. 1) in Fig. C.1. As we see, the artificial slits are placed either parallel or near parallel to the loops that are most likely in the foreground of the DFs. Such placement of slits also makes sure that the trajectories we find in the X-T plots (Figs. 2 and 3) are not signatures of kink oscillations (Verwichte et al. 2004; Anfinogentov et al. 2015; Okamoto & De Pontieu 2011; Mandal et al. 2022). This is because during kink oscillations, a loop sways sideways – thus, to capture these kink oscillations in an X-T map, we must place the slit perpendicular to the loop, not parallel to it. Hence, the tracks we find in X-T maps are due to motions of blob-like DFs (as discussed below) and not related to transverse oscillations.

In Figs. C.2 and C.3, we present two illustrative examples of DF evolution across channels. Furthermore, we also provide animations associated with this figure that shows the complete evolution of these DFs over their lifetime. As seen from the figure, a bright blob-like feature moves back and forth with time and therefore, creating parabolic tracks in X-T maps. The feature appears more diffuse and elongated in IRIS 2796 channel in comparison to other passbands. Moreover, it is best identified in EUV and IRIS 1400 data, while in the AIA 171 data, it can be identified in hindsight, namely, after spotting it in the EUV images. Therefore, we conclude that although there are co-spatial and co-temporal signatures of DFs from the chromosphere to the corona, their detection is generally limited by the resolution of the data used to investigate them.

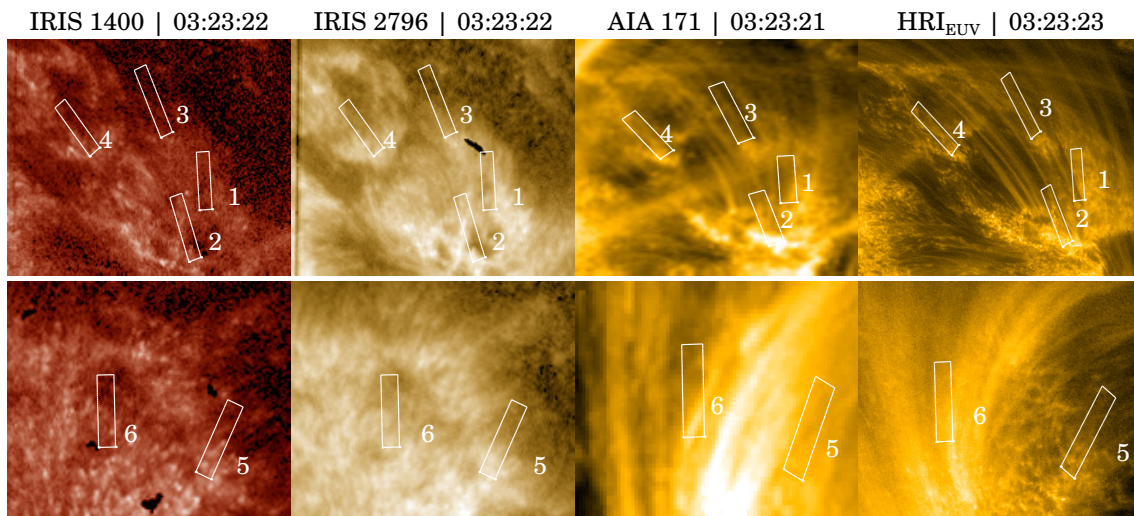


Fig. C.1. A zoomed-in view of Fig. 1.

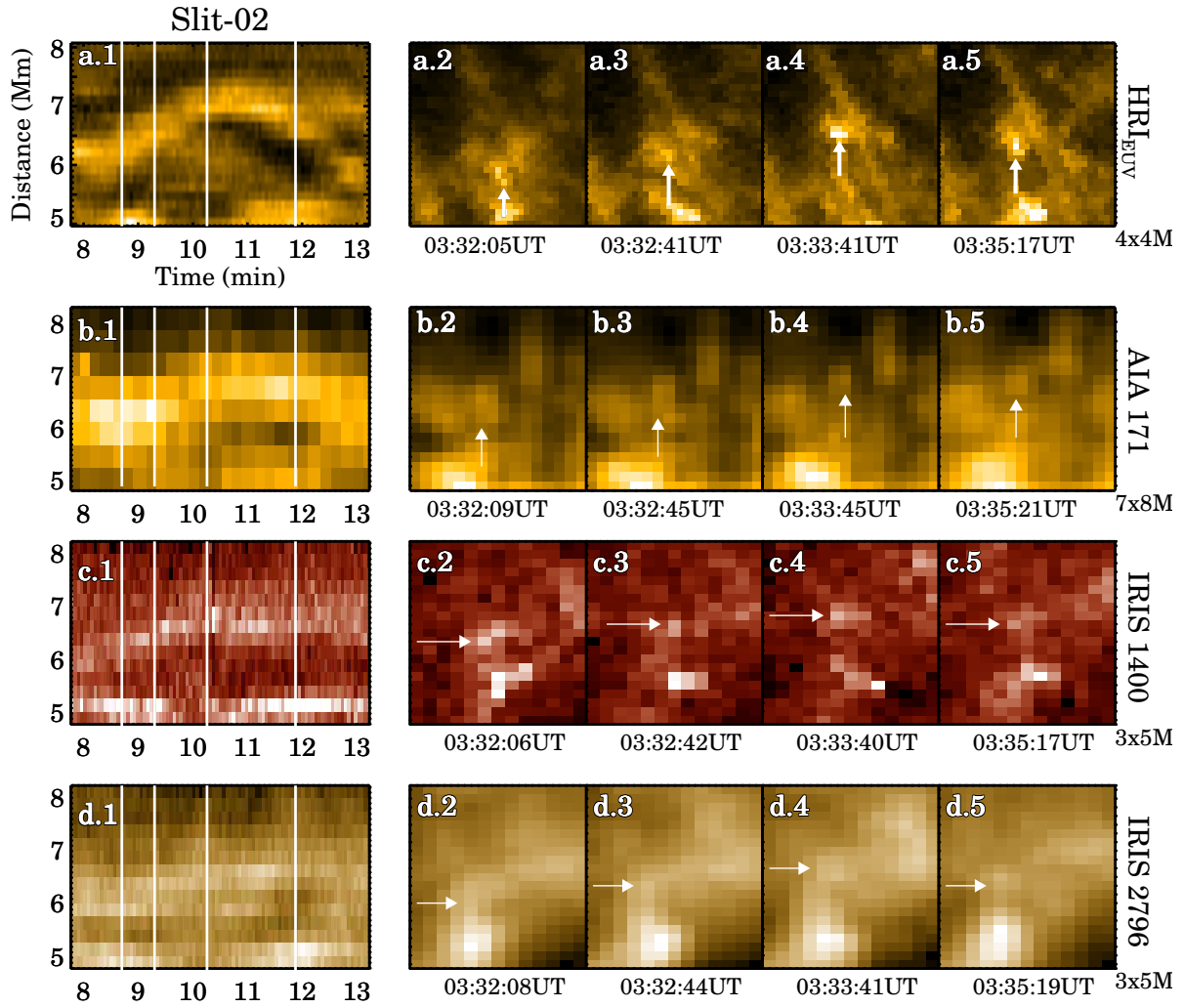


Fig. C.2. Evolution of a DF (from slit-02) across channels. Panel a.1 shows the bright (parabolic) track that the DF creates in the EUV X-T map. The four vertical lines mark the time stamps of snapshots in panels a.2, a.3, a.4, and a.4, in which the white-arrows point toward the instantaneous position of the DF. Panels b-d have the same format but for AIA 171 Å, IRIS 1400 Å, IRIS 2796 Å observations. An animated version of this figure is available [online](#).

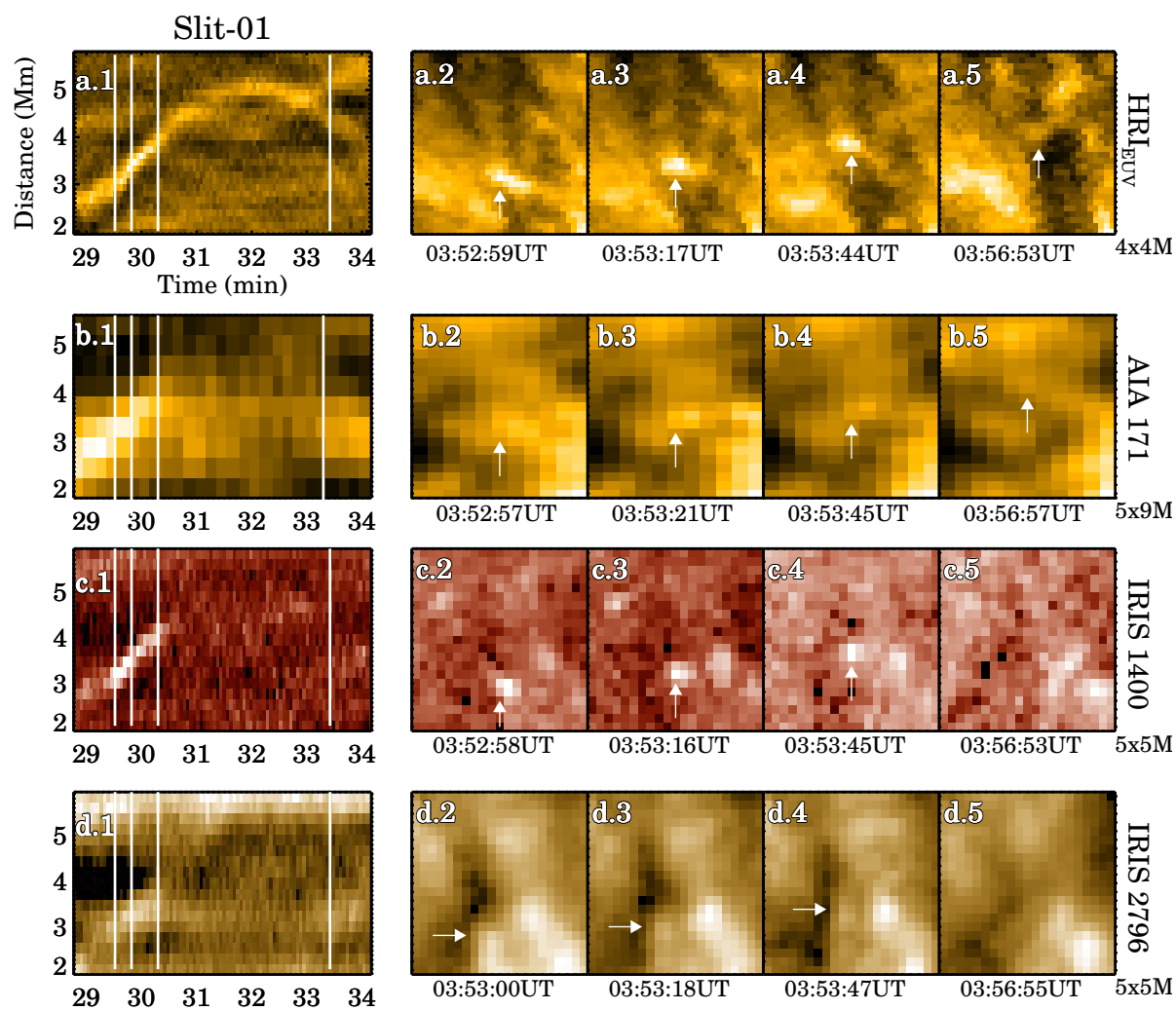


Fig. C.3. Similar to Fig. C.2 but for a DF from slit-01. An animated version of this figure is available [online](#).

Appendix D: Co-alignment between instruments

As explained in Sect. 2, we used WCS keywords to co-align data from HRI_{EUV}, AIA, and IRIS. Figure D.1 provides a visual representation of such aligned data. The HRI_{EUV} and AIA images

are scaled to the IRIS resolution for easy comparison. Following the contours (derived from the HRI_{EUV} intensity, panel c), we find that the bright, low-lying regions in all four channels overlap well, while large fan-loops appear somewhat different.

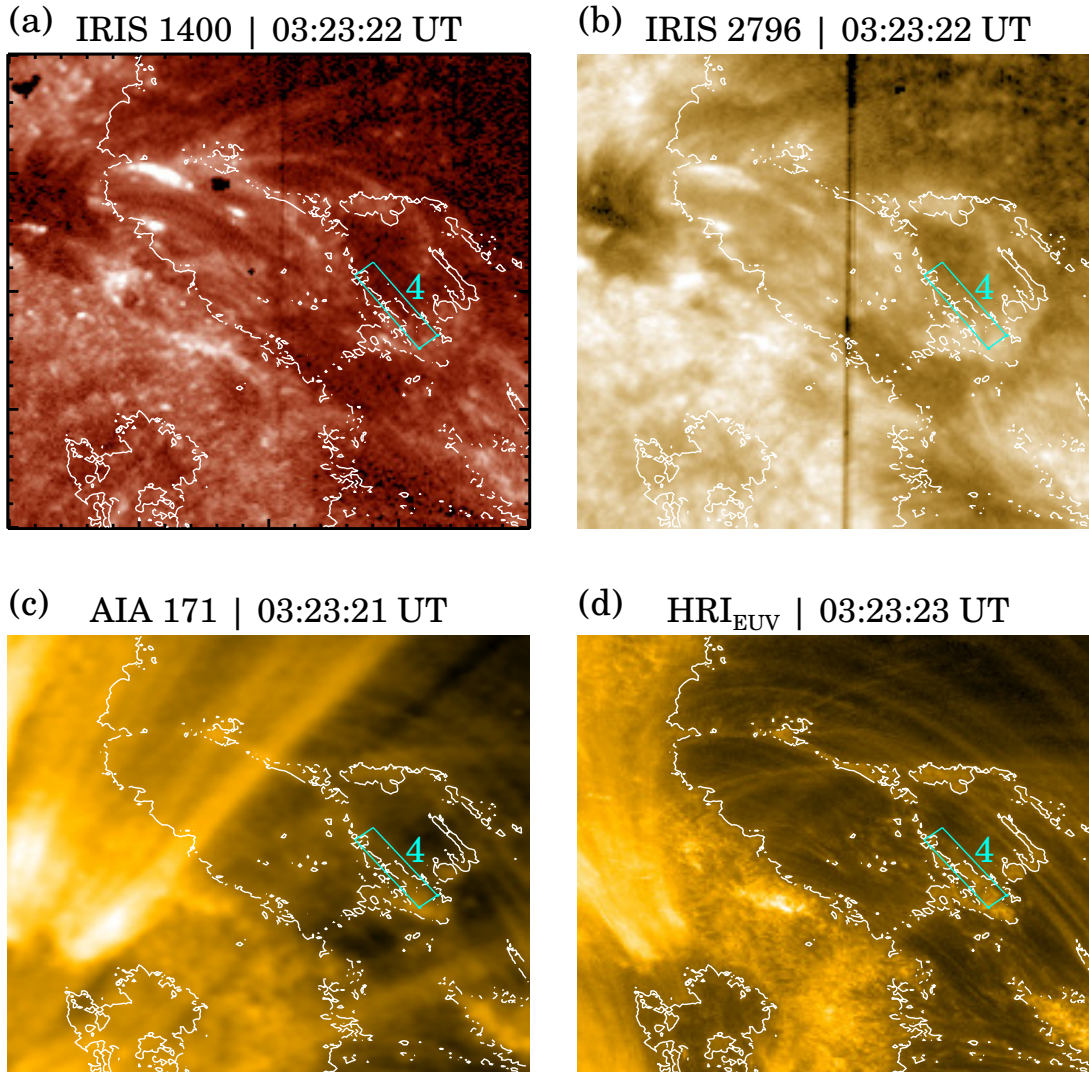


Fig. D.1. Co-aligned datasets from IRIS (panels a-b), AIA (panel c), and HRI_{EUV} (panel d). All four panels of this figure represent a small section of the full FoV, as highlighted by the yellow box in Fig. 1b. The AIA and HRI_{EUV} images are scaled to IRIS pixel scale. The contours overlotted on every panel are derived using intensities from the HRI_{EUV} image (panel d). Slit-4 that falls within this FoV is shown as the cyan box in every panel.

Appendix E: X-T maps with colourbars

In Figs. E.1 and E.2, we present X-T maps (of Figs. 2 and 3) with colourbars for the ease of following the observed intensity changes. Again, we emphasise that these maps are background

subtracted (as calculated through a boxcar smoothing along the transverse direction, namely, along the y-axis of an X-T map). Therefore, the colourbars represent the relative change defined as: $(\text{map} - \text{map}_{\text{smoothed}}) / \text{map}_{\text{smoothed}}$.

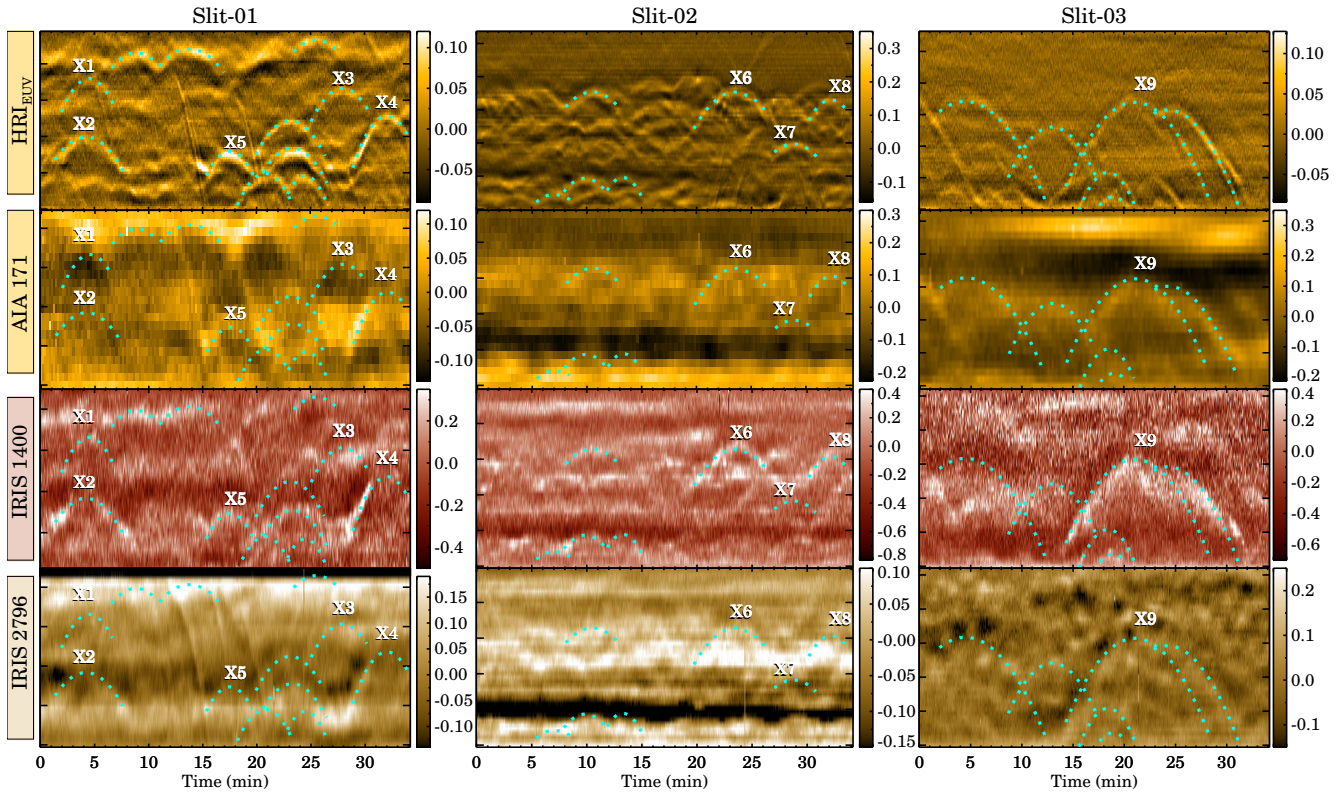


Fig. E.1. Same as Fig. 2m but with colourbars that outline the relative change, as described in Sect. E.

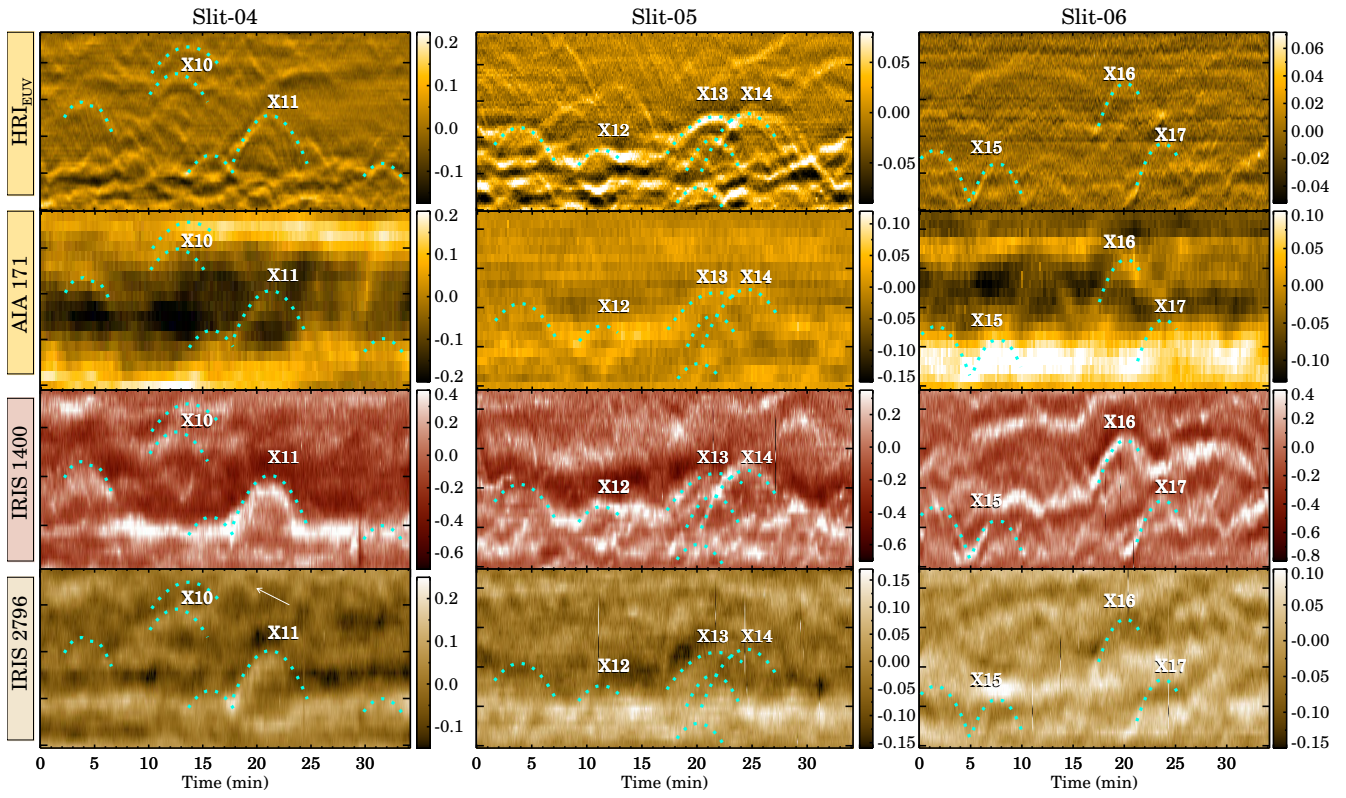


Fig. E.2. Same as Fig. 3 but with colourbars that outline the relative change as described in Sect. E.